

First-principles study of Bi³⁺-related luminescence and traps in the perovskites CaMO₃ (M = Zr, Sn, Ti)

Bibo Lou^{1,2}, Jun Wen,³ Jiajia Cai², Yau-Yuen Yeung^{4,*}, Min Yin,^{2,†} and Chang-Kui Duan^{1,‡}

¹Hefei National Laboratory for Physical Sciences at the Microscale and School of Physical Sciences, University of Science and Technology of China, Hefei 230026, China

²CAS Key Laboratory of Strongly-Coupled Quantum Matter Physics, University of Science and Technology of China, Hefei 230026, China

³School of Electronic Engineering and Intelligent Manufacturing, Anqing Normal University, Anqing 246133, China

⁴Department of Science and Environmental Studies, the Education University of Hong Kong, 10 Lo Ping Road, Tai Po, NT, Hong Kong, China



(Received 26 October 2020; accepted 22 January 2021; published 3 February 2021)

The Bi³⁺ ion is an excellent activator and sensitizer for luminescent materials. However, the complexity and variety of the Bi³⁺-related transitions bring a great challenge to the study of luminescence processes of Bi³⁺ doped materials. Here, we presented first-principles calculations to determine the excitation, relaxation, and emission processes of Bi³⁺ activated materials by using CaMO₃ : Bi³⁺ (M = Zr, Sn, Ti) as prototype systems, where Bi³⁺ substitutes Ca²⁺ in similar coordinate environments but presents tremendously different excitation and emission spectra. The equilibrium geometric structures of excited states were calculated based on density-functional theory (DFT), with appropriately constraining the electron occupation and including the spin-orbit couplings. Then the hybrid DFT calculations were carried out to obtain the electronic structures and defect levels. Different metastable excited states and Stokes shift were obtained for M = Zr, Sn, and Ti, which explain the remarkable differences in the measured emission spectra. The energies of three types of transitions are obtained from the calculations, including intra-Bi³⁺ bands transition and charge transfer between Bi³⁺ ions and the band edges. This leads to a clear and reliable interpretation of all the excitation spectra in the series. The method and its applications to CaMO₃ : Bi³⁺ show the potential of first-principles calculations in analyzing and predicting luminescent properties of Bi³⁺ activated materials.

DOI: [10.1103/PhysRevB.103.075109](https://doi.org/10.1103/PhysRevB.103.075109)

I. INTRODUCTION

Bi³⁺ doped materials can produce ultraviolet to red luminescence in different hosts, which exhibit various potential applications, such as solid-state lighting and display [1–3], optical fiber lasers [4], biomedicine [5], and optical sensing [6]. In recent years, the dramatically increased research interest also shows the importance of the bismuth activated materials [7]. The possible underlying photoluminescent mechanisms and the strategies for phosphor design have been discussed in several recent review articles [7–9]. The Bi³⁺ ion has a (6s)² outer electron configuration with ¹S₀ ground state. A strong absorption band located in the vacuum ultraviolet region is usually attributed to the (6s²) ¹S₀ → (6s6p) ¹P₁ (C band) transition, whereas the generally measured excitation and emission bands are attributed to the transition between (6s²) ¹S₀ and (6s6p) ³P₁ (A band in Fig. 1), which is enabled by spin-orbit coupling (SOC) [10]. Except for the transition between two electron configurations of a Bi³⁺ ion, Fig. 1 also plots the excitation and emission processes involving charge transfer between a Bi³⁺ ion and the host, such as the valence band (VB) to Bi³⁺ charge transfer, usually denoted as CT [8,9]. And the ionization of an electron from Bi³⁺

to the conduction band (CB), usually denoted as metal-metal charge transfer (MMCT) [8,9]. All those processes in Bi³⁺ are electric dipole transitions in nature, although magnetic dipole transitions can be important for low valent bismuth dopants. Experimental studies have been carried out for many Bi³⁺ activated luminescent materials and the excitation and emission spectra have been analyzed with empirical models [11–15] or the guidance of band structure calculations [16,17]. However, there remain ambiguities in the analyses due to the difficulties in predicting reliable energies of Bi³⁺ excited states and their relative positions with respect to the band edges of the host [8]. This makes the design and optimization of Bi³⁺-activated materials challenging.

In order to reveal the luminescence mechanisms of different Bi³⁺ doped phosphors, Awater and Dorenbos introduced a set of vacuum referred binding energy (VRBE) diagrams, which exhibited the binding energy of the electron in the valence and conduction bands, as well as in the 6s ground and 6p excited states in 117 different inorganic compounds and provided insight into the physical properties of the Bi³⁺ activator ion in different chemical environments [11]. Boutinaud *et al.* introduced a criterion assisting the Bi³⁺-related excitation spectra assignments [13–15]. Taking into account the structural characteristics of the hosts, the anion relaxation and environmental factor, this criterion allows an estimation of the Bi³⁺-related excitation bands. Recently, Back *et al.* have studied Bi³⁺-activated CaMO₃ : Bi³⁺ perovskites (M = Zr, Sn, Ti) to investigate the origin of the

*Corresponding author: yuyeung@eduhk.hk

†Corresponding author: yinmin@ustc.edu.cn

‡Corresponding author: ckduan@ustc.edu.cn

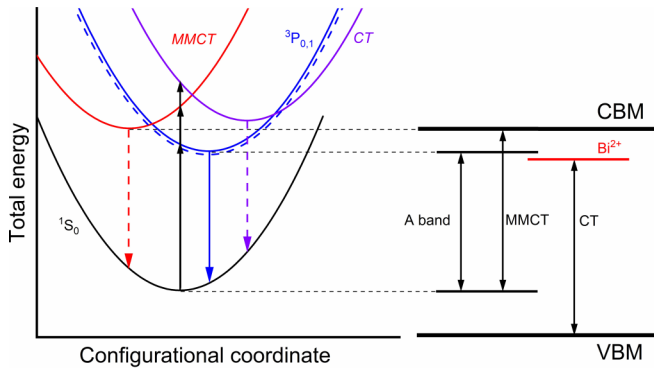


FIG. 1. Left: schematic configuration coordinate diagram of the excitation and emission involving A band, the lowest MMCT and CT states; right: thermodynamic charge transition levels, with double directional arrows showing the transitions zero-phonon lines.

luminescence experimentally together with above empirical models [12]. It is very interesting that, despite great similarity in geometric structure and coordinate environment, the emission of Bi^{3+} in these three hosts and their corresponding excitation spectra show tremendous differences in the peak position and the band broadening [18–21]. The rich experimental phenomena in the $\text{CaMO}_3 : \text{Bi}^{3+}$ series provide a good prototype for a systematic theoretical study of the luminescent processes of Bi^{3+} activated materials.

First-principles calculations have played a crucial role in studying the luminescence of the rare-earth ions, such as Eu^{2+} and Ce^{3+} , and provided accurate information about the transition energies and Stokes shifts with methods based on DFT and analysis of the system energies [22–24]. In recent years, advanced calculations based on the hybrid DFT have improved the predictions of chemical and electronic properties of materials with activators [25]. For the Bi^{3+} activated phosphors, previous first-principles studies of the band-structure type calculations have limited capacity in analyzing and interpreting experimental results [16,17]. It has been realized that effectively theoretically modeling the luminescent processes and optical performance of Bi^{3+} doped materials is important but very challenging [8]. The greatly underestimated band gap in the conventional DFT calculations strongly affected the analyses of optical transitions of dopants and defects. Meanwhile, for systems containing heavy ion Bi^{3+} , the large relativistic effects, both scalar and spin-orbit coupling, and the correlation of valence electrons bring difficulties in the DFT calculations. In connection to the optical transitions of Bi^{3+} activators, the excited states calculations remain the greatest challenge in their luminescence mechanism studies.

Here, we presented first-principles calculations to determine the excitation, relaxation, and emission processes of Bi^{3+} activated materials by using $\text{CaMO}_3 : \text{Bi}^{3+}$ ($M = \text{Zr}, \text{Sn}, \text{Ti}$) as prototype systems due to rich experimental phenomena and data [12,18–21]. The atomic geometric structures and electronic properties of both the ground and excited states were obtained. The obtained excitation and emission processes and energies agree very well with experimental results. A clear picture of all the levels at both ground and excited equilibrium geometric structures was

constructed. It shows the potential of first-principles calculations in analyzing and predicting properties of Bi^{3+} activated luminescent materials, which will benefit the design and optimization of new phosphors.

II. METHODOLOGY

A. Parameter settings

The crystal structure of CaMO_3 ($M = \text{Zr}, \text{Sn}, \text{Ti}$) compounds belongs to the orthorhombic distorted perovskite structure with the space group $Pbmn$ [21]. In our calculation, the Bi-doped CaMO_3 crystals were modeled using a $2 \times 2 \times 2$ defective supercell containing 160 atoms. Structural optimization was carried out with DFT calculations, and the Perdew-Burke-Ernzerof (PBE) exchange-correlation functional within generalized gradient approximation was selected, as implemented in the Vienna *ab initio* Simulation Package (VASP) [26,27]. The projector augmented wave (PAW) pseudopotentials [28] were adopted to describe the interactions of elements, where the valence configurations of Ca, Ti, Sn, Zr, O, and Bi are $3s^2 3p^6 4s^2$, $3s^2 3p^6 3d^2 4s^2$, $4d^{10} 5s^2 5p^2$, $4s^2 4p^6 4d^2 5s^2$, $2s^2 2p^4$, and $5d^{10} 6s^2 6p^3$ respectively. A plane-wave basis set with an energy cutoff of 400 eV was adopted. For the initial unit cell, much larger $7 \times 5 \times 7$ k points grids were employed to optimize the unit cell before the band structure calculation. As for supercell, the k -point Γ was used to sample the Brillouin zone. Based on our tests using 520-eV cutoff energy and $3 \times 3 \times 3$ k -point grids, the errors in transition levels and excitation and emission energies are less than 0.1 eV. The dispersion of the defect level of bismuth dopant in the supercell Brillouin zone shows that interaction between neighboring dopants is small and the size of the supercell is sufficient. Evidence of this is provided in Fig. S1 of the Supplemental Material (SM) [29]. The ionic positions were fully relaxed until the residual force acting on each ion was less than 0.01 eV/Å. In the calculation of the band structures, the point coordinates of the high symmetry k path G, Z, T, Y, S, X, U , and R in the Brillouin zones were chosen for K points [37]. For comparison, the band gap was also calculated by utilizing the Tran–Blaha modified Becke–Johnson exchange potential approximation (TB-mBJ) method [38] with the WIEN2K package [39]. The valance band maximum (VBM) alignment of the three hosts relative to the vacuum state were obtained by PBE calculations on a slab for each host. The slab contains $2 \times 1 \times 1$ unit cells with 40 atoms and a vacuum layer of 30 Å along the a axis.

B. Defect level calculations

Hybrid DFT, which includes a portion of Hartree-Fock exchange α [40], has emerged as a useful method to improve the calculations of the band structure and defect levels for many semiconductors and insulators. The required content of Hartree-Fock exchange α has been shown approximately the inverse of the optical dielectric constant for excellent description of the electronic structure of both the perfect crystal and a broad range of defects in wide-gap oxide semiconductors [41–43]. By following this empirical relation, we took $\alpha = 15\%$ for CaTiO_3 (denoted as PBE015 hereafter), $\alpha = 25\%$ for

CaSnO₃ (PBE025), and $\alpha = 20\%$ for CaZrO₃ (PBE020) in the PBE0 calculation, without fine tuning α values to suit the measured band gaps. Because of the large SOC in the Bi²⁺ and the ³P_{0,1} excited state of Bi³⁺, hybrid DFT + SOC calculations were applied in the calculations [44]. The formation energy of a defect X in the charge state of q can be derived as follows:

$$E^f(X^q, E_F) = E_{\text{tot}}[X^q] - E_{\text{tot}}[\text{bulk}] - \sum_i n_i \mu_i + qE_F, \quad (1)$$

where E_{tot} is the total energy of the optimized supercells, n_i are the numbers of the atoms of elements i which are added to ($n_i > 0$) and or removed from ($n_i < 0$) the perfect supercell [45], and μ_i are corresponding chemical potentials of these species. The Fermi energy level E_F represents the chemical potential of the electrons. For the energy corrections in the DFT computations for the supercells containing charge defects, including the image charge interaction corrections and potential alignments, Durrant *et al.* proposed that the combination of the Lany-Zunger correction for the defect energy due to image charge and the potential alignment between the two neutral systems (the original host supercell and the unrelaxed defect containing supercell) can yield accurate corrections [33]. In our calculations of the Bi³⁺ induced defect levels and the formation energies of CaMO₃:Bi³⁺ ($M = \text{Zr, Sn, Ti}$), the charge corrections are all the level of 0.1 eV or less. More details of the charge corrections can be found in Note 1 of the Supplemental Material [29]. The thermodynamic charge transition level $\epsilon(q_1/q_2)$ was utilized to predict the positions of defect levels, and it is defined as the Fermi level at which the defect formation energies of X^{q_1} and X^{q_2} equal each other. It can be deduced from Eq. (1) as

$$\epsilon(q_1/q_2) = \frac{E_{\text{tot}}(\{X^{q_1}\}_{q_1}) - E_{\text{tot}}(\{X^{q_2}\}_{q_2})}{q_2 - q_1}. \quad (2)$$

C. Excited state optimizations

There are three types of excited states for Bi³⁺ in crystals: the so called MMCT (Bi⁴⁺ + e_{CB}), CT (Bi²⁺ + h_{VB}), and the A band (³P_{0,1}) excited states. Since an extra extended electron or hole in the energy band of the host has little impact on the local geometric structure of the defect, the equilibrium structure for MMCT and CT type excited states were approximately obtained by geometry optimization for the supercell with electron number setting corresponding to Bi⁴⁺ and Bi²⁺ using PBE functional. The calculation of the equilibrium structure of the ³P_{0,1} state is much more involved. The ³P_{0,1} state is expected to be the lowest excited state of the defect, so it can be calculated by constraining the spin multiplicity when SOC is not included. However, SOC needs to be taken into account, since it can affect the relative position of the ³P_{0,1} and other excited states. With the inclusion of SOC, geometry optimization can be performed by moving an electron from the nominal 6s_{1/2} KS orbital to 6p_{1/2}.

The geometric structures of the lowest excited state in all the three CaMO₃:Bi³⁺ are readily calculated, but it can be troublesome to determine them for other excited states. Due to the small band gap in CaTiO₃, the Bi³⁺ 6p KS orbitals are high up in CB. In the PBE calculation of CaTiO₃:Bi³⁺, even after the SOC of Bi³⁺ has been included, the Bi³⁺-6p KS

orbitals remain scattered and high up in the CB. Thus one of the Bi³⁺ 6s electrons could hardly be promoted to occupy the lowest 6p KS band to form the excited state (Bi³⁺)*. In the case of the CT excited state in CaTiO₃, the electron excited from the VB cannot be constrained to occupy the Bi³⁺-6p KS orbital to form Bi²⁺ either. Thus, in CaTiO₃:Bi³⁺, only the atomic configuration of the lowest excited state, i.e., the MMCT state, is obtained. As for CaSnO₃, the band gap is larger than that of CaTiO₃, but Bi³⁺-6p KS orbitals remain slightly higher than the conduction band minimum (CBM) in the PBE + SOC calculations. Although the equilibrium structure of (Bi³⁺)* cannot be obtained by setting spin multiplicity, the original Bi³⁺ 6s electron can be lifted to occupy the lowest 6p KS band by adding two extra electrons to the CB in the constrained DFT calculation.

D. Calculation of excitation and emission energies

Based on the Franck-Condon principle, the peak energy for excitation or emission for a given transition can be obtained by the differences of the total energies of the excited and ground electronic state at the equilibrium geometric structure of the initial electronic states of the transition. Since the excited state of the MMCT excitation is composed of Bi⁴⁺ and an electron in CB, the MMCT excitation energy is approximated by the difference of the energy of the CaMO₃:Bi⁴⁺ system plus an electron in CBM from that of the CaMO₃:Bi³⁺ system, i.e.,

$$\epsilon_{\text{MMCT}} = [\epsilon_{\text{CBM}} + E_{\text{tot}}(\{\text{Bi}^{4+}\}_{3+})] - E_{\text{tot}}(\{\text{Bi}^{3+}\}_{3+}). \quad (3)$$

Here the two total energies with subscript “3+” are calculated at the CaMO₃:Bi³⁺ ground state geometric structures. The corrections to ϵ_{MMCT} due to the Coulomb interaction between Bi⁴⁺ and the electron in CB were taken into account together with charge corrections (Table S3 in the SM [29]). The MMCT emission is calculated similarly but at the equilibrium structure of CaMO₃:Bi⁴⁺ by neglecting the impact of the extra itinerant electron in CB. Similarly, the CT absorption and emission energies can be calculated as the difference of the energy of CaMO₃:Bi²⁺ plus a hole from that of CaMO₃:Bi³⁺ system, also by following the Frank-Condon principle, i.e.,

$$\epsilon_{\text{CT}} = [E_{\text{tot}}(\{\text{Bi}^{2+}\}_{3+}) - \epsilon_{\text{VBM}}] - E_{\text{tot}}(\{\text{Bi}^{3+}\}_{3+}). \quad (4)$$

In principle, the excitation and emission energies for the A band can also be calculated as the difference of the total energy of the initial and final states. Actually, we calculated these transition energies using the PBE functional with or without including SOC and obtained their differences, which were then used to account for the SOC contribution to the transition energies of hybrid DFT.

III. RESULTS AND DISCUSSION

A. Properties of the hosts

The calculated lattice parameters and volumes for the three pristine CaMO₃ hosts are very close to those from experiments (Table I), with differences in lattice parameters mostly less than 0.5% for CaTiO₃ and CaZrO₃ and no more than 1% for CaSnO₃. In all three hosts, Ca ions locate at Wyck. 4c sites inside of a distorted cube of eight MO₆ groups [Fig. 2(a)].

TABLE I. Comparison of the PBE calculated with measured lattice parameters (Å) of CaMO_3 .

	Calculated				Experimental ^a			
	<i>a</i>	<i>b</i>	<i>c</i>	volume	<i>a</i>	<i>b</i>	<i>c</i>	volume
CaTiO_3	5.358	5.449	7.621	222.52	5.381	5.442	7.641	223.76
CaSnO_3	5.531	5.692	7.910	249.07	5.482	5.638	7.839	242.31
CaZrO_3	5.567	5.758	7.994	256.24	5.583	5.759	8.007	257.45

^aThe experimental data come from Refs. [18,19,50].

As shown in Fig. 2(b), the Ca ion has 12 oxygen ligands, but four of them have bond lengths exceeding 3 Å and will not be counted as the ligands of Ca in our analysis. PBE calculations predict band gaps of 2.43, 2.59, and 4.06 eV for $M = \text{Ti}$, Sn , and Zr , respectively, which are seriously underestimated, as the host band excitation peaks are at 3.78, 4.79, and 5.70 eV [12]. Hybrid DFT calculations with appropriate parameters lead to improved band gaps of 3.72, 4.85, and 5.94 eV, which are comparable to the band gaps of 3.57, 4.99, and 5.54 eV obtained by utilizing the TB-mBJ method [38] with the WIEN2K package [39]. The PBE band structures (with band gaps corrected by hybrid DFT) are plotted in Fig. 3. It shows that the CaTiO_3 and CaZrO_3 are both direct band gap insulators, while CaSnO_3 is an indirect band gap material with the CBM and the VBM located at the high symmetry k point of G and S respectively. The CaTiO_3 and CaZrO_3 are both direct band gap insulators, while CaSnO_3 is an indirect band gap material with the CBM and the VBM located at the high symmetry k point of G and S respectively. In CaSnO_3 host, the CB at the Γ point is less flat than that in CaTiO_3 and CaZrO_3 , meaning a lower effective mass of the electron. The computed densities of states (DOSs) show that the top of VBs for all the three CaMO_3 are dominated by the Op orbitals, and the compositions of CB are dominated by the s or d orbitals of M^{4+} ions. The bottoms of CBs of CaTiO_3 and CaZrO_3 are similar and both dominated by the $M d$ orbitals, in contrast to CaSnO_3 , where Sns and Op hybrid orbital are dominant.

B. Ground and excited states of $\text{CaMO}_3 : \text{Bi}^{3+}$

The mean distances between the Ca atom and their eight nearest-neighbor O atoms are 2.495, 2.529, and 2.556 Å for CaTiO_3 , CaSnO_3 , and CaZrO_3 , respectively. Due to the similarity in ionic radii and chemical properties, the incorporated Bi^{3+} (ion radius $r = 1.03$ Å, coordination number CN = 6; $r = 1.17$ Å, CN = 8) ions tend to substitute the Ca^{2+} ($r =$

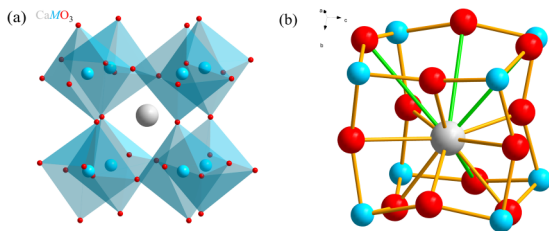


FIG. 2. (a) Crystalline structure of CaMO_3 orthorhombic distorted perovskite. (b) Polyhedron diagram of Ca^{2+} site in CaMO_3 , which is coordinated with 12 oxygen atoms, with four oxygen ligands of bond lengths are more than 3 Å showing in green.

1.12 Å, CN = 8) sites (denoted as Bi_{Ca}), rather than Ti^{4+} ($r = 0.605$ Å, CN = 6), Sn^{4+} ($r = 0.69$ Å, CN = 6), or Zr^{4+} ($r = 0.72$ Å, CN = 6) sites in the three hosts. This is also confirmed by our calculation that the formation energies of Bi_M^{1-} , i.e., Bi^{3+} replacing M^{4+} ($M = \text{Ti}$, Sn , Zr), are substantially larger than $\text{Bi}_{\text{Ca}}^{1+}$ (Bi^{3+} replacing Ca^{2+}) under relevant chemical conditions. The details can be found in Fig. S3 of the SM [29]. The charge compensation can be fulfilled by negatively charged calcium vacancies $\text{V}_{\text{Ca}}^{2-}$, but its effect on the excitation and emission energies is negligible in the case of low dopant concentration. Direct calculations show that there is no tendency of Bi_{Ca} and V_{Ca} clustering, and so we do not include the charge compensation in our supercell calculations but will take charge corrections into account instead. In CaTiO_3 and CaZrO_3 , the oxygen environments are hardly changed by Bi^{3+} substitution (Table II) in that the mean bond lengths change by less than 0.002 Å, while in CaSnO_3 the oxygen environments change slightly by Bi^{3+} substitution, resulting in a decrease in mean bond length by 0.015 Å (Fig. S4 in the SM [29]).

It is noted that, although the MMCT of Bi^{3+} to host cation or CB has been denoted as $\text{Bi}^{3+} \rightarrow \text{Bi}^{4+} + e_{\text{CB}}$, the electron is actually removed from an antibonding orbital contributed by bismuth $6s$ atomic orbital and oxygen $2p$ atomic orbital, as plotted in Fig. S5 in the SM [29]. Similarly, in A band transition, an electron is lifted from such an antibonding orbital to a bismuth $6p$ orbital according to our calculations. Comparing with the ground states, the excited states structure relaxations show clear changes in the bond lengths, as shown in Fig. S6 of the SM [29]. The mean bond lengths of Bi-O in the MMCT states decrease about 3% (~ 0.07 Å in CaTiO_3 and ~ 0.08 Å in CaSnO_3 and CaZrO_3), as listed in Table II. It is interesting that the variation of bond lengths is far from an overall shrinkage but dominated by the decrease in length of three bonds, which is ~ 0.20 Å in CaZrO_3 and ~ 0.13 Å in CaSnO_3 , while in CaTiO_3 , there are five oxygen ligands whose bond length decrease by ~ 0.10 Å, as shown in Table S4 in the SM [29]. For CT states, we obtained the equilibrium configurations in CaSnO_3 and CaZrO_3 , and the mean bond lengths of Bi-O increase by about 7% (~ 0.18 Å) compared to the ground states. The three oxygen ligands, which are sensitive during the structure variation from the ground state to the MMCT state, remain the most sensitive ones and their bond lengths increase by ~ 0.31 Å from the ground state to the CT state for CaZrO_3 and CaSnO_3 . Meanwhile, there are three other oxygen ligands whose bond lengths increase more than ~ 0.10 Å in the CT state. For the $(\text{Bi}^{3+})^*$ excited state (${}^3P_{0,1}$), the mean bond length of CaZrO_3 increases by 5.0% (~ 0.13 Å) and 3.3% (~ 0.08 Å) in CaSnO_3 . The changes in

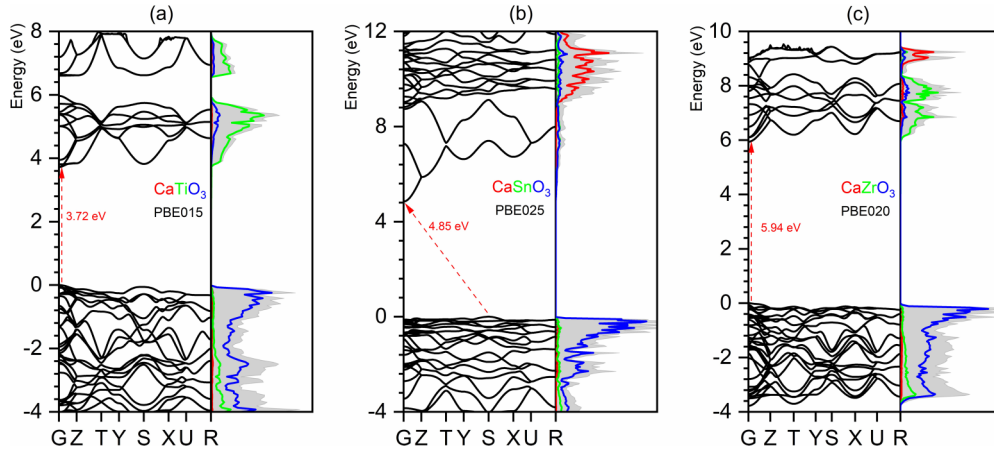


FIG. 3. PBE calculated band structures, with band gaps taken from hybrid DFT calculation for pristine hosts: (a) CaTiO_3 , 3.72 eV; (b) CaSnO_3 , 4.85 eV; (c) CaZrO_3 , 5.94 eV, and the corresponding total or partial densities of states shown as DOS and colored PDOS, respectively.

bond lengths are dominated by the four outermost oxygen ligands in both CaSnO_3 (~ 0.17 Å) and CaZrO_3 (~ 0.23 Å). In short, different from the expectation of a dominant overall variation of all the Bi-O bond lengths over the ground state geometry structure, some bond lengths vary dramatically while others are barely changed.

In hybrid DFT calculations, the transition energies of the lowest excitation and emission are always readily calculated. Only in $\text{CaZrO}_3:\text{Bi}^{3+}$ all the higher excitation energies and the emission energy were obtained by straightforward calculations. In the case of $\text{CaTiO}_3:\text{Bi}^{3+}$, due to the smaller band gap, we could not obtain the equilibrium structures of the higher CT and $^3P_{0,1}$ excited states. Similar problem also occurred in the higher $^3P_{0,1}$ state in $\text{CaSnO}_3:\text{Bi}^{3+}$. A proper mixing parameter α can produce improved band gap energies, and by assuming approximately the generalized Koopmans theorem [46], the hybrid DFT calculation is also able to give a consistent description for localized defects [43]. We utilized the eigenvalues in hybrid DFT calculation, the so-called generalized Kohn-Sham (GKS) eigenvalues as an approximation for determining the transition energies [see Fig. S7 for the detailed partial DOS (PDOS) diagram] [25]. The energy difference between the unoccupied $6s$ and $6p$ KS orbitals were applied to approximate the A band excitation energy in Bi-doped CaTiO_3 . For CaSnO_3 , this approximation was also available in the emission energy since we obtained the equilibrium geometric structure of the excited state. The CT excitation in Bi-doped CaTiO_3 and CaSnO_3 was approx-

imated with the energy difference between the VBM and lowest unoccupied $6p$ KS orbital in CaMO_3 . The CT excitation in CaSnO_3 was approximated with GKS eigenvalues, while the emission was calculated with Eq. (4) since the optimized $\text{CaSnO}_3:\text{Bi}^{2+}$ structure was obtained. The validity of the approximations in our Bi^{3+} -related excited state calculations will be scrutinized by the comparison of the calculated excitation and emission energies to the experimental results.

C. Bi^{3+} -related defect levels

In order to compare the Bi^{3+} induced defect levels in three materials, the VBM was aligned relative to the vacuum level as plotted in Fig. 4, whereas the data are listed in Table S5 of the SM [29]. The doped Bi^{3+} ions can work as hole traps in all three CaMO_3 . The depth of the hole trap is found to be the largest in CaSnO_3 (1.39 eV), whereas it is 0.99 eV in CaTiO_3 and 1.12 eV in CaZrO_3 . In CaSnO_3 , the bond lengths between Ca^{2+} ions and their surrounding oxygen ions are looser than those in CaTiO_3 and CaZrO_3 after Bi^{3+} substitution, allowing a larger structure relaxation and nephelauxetic effects, which leads to a larger trap depth. Our results differ remarkably from the VRBE diagram for $\text{CaMO}_3:\text{Bi}^{3+}$ in Ref. [12], where the depth of the Bi^{3+} $6s$ hole trap in CaZrO_3 differs from that of

TABLE II. Calculated mean bond lengths of Ca-O and Bi-O in units of Å.

System	$\text{Ca}^{2+}\text{-O}^a$	$\text{Bi}^{3+}\text{-O}$	$(\text{Bi}^{3+})^*\text{-O}$	$\text{Bi}^{4+}\text{-O}$	$\text{Bi}^{2+}\text{-O}$
CaTiO_3	2.495	2.497		2.429	
CaSnO_3	2.529	2.514	2.597	2.431	2.696
CaZrO_3	2.556	2.555	2.682	2.475	2.734

^a Ca^{2+} and Bi^{3+} represent the host Ca^{2+} site and the dopant site, respectively. $(\text{Bi}^{3+})^*$, Bi^{4+} , and Bi^{2+} are the optimized A band, MMCT, and CT excited states for the Bi^{3+} dopant, respectively.

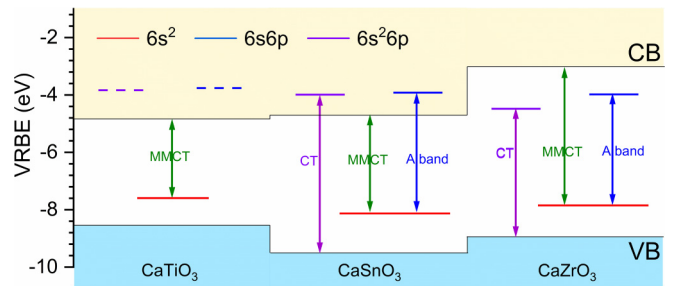


FIG. 4. The VRBE of Bi^{3+} induced defect levels and their zero-phonon transitions relative to the VBM in CaMO_3 perovskites ($M = \text{Zr}, \text{Sn}, \text{Ti}$) calculated with hybrid DFT, where solid lines represent thermodynamic charge transition levels and dash lines represent optical charge transition levels. The VBM by hybrid DFT calculation is aligned relative to the vacuum state.

CaTiO₃ by more than 2 eV. The bottom of CBs is dominated by the M^{4+} orbitals, and this leads to the dependence of the band gaps on M ions. As a result of a small band gap, the CBM positions of CaTiO₃ and CaSnO₃ are both beneath the thermodynamic charge transition level $\epsilon(+1/0)$ of the Bi_{Ca}, making Bi²⁺ unstable. However, the $\epsilon(+1/0)$ of Bi_{Ca} in CaZrO₃ is beneath the CBM, leading to an electron trap at -1.46 eV relative to the CBM.

Although the structures are similar in all three hosts, the different M^{4+} cation has some impact on the relative position of the VBM relative to the vacuum state, which is shown in Fig. S8 of the SM [29]. The VRBE of the VBM in CaSnO₃ is about -1.00 eV lower relative to that in CaTiO₃ and -0.56 eV lower relative to that in CaZrO₃. The VRBE of the $\epsilon(+2/+1)$ of Bi_{Ca}, i.e., the energy position of the hole trap of $6s$ character of the bismuth ion, are similar in all three hosts, with only the lowest being in CaSnO₃:Bi³⁺, which is -0.4 to -0.3 eV relative the other two. Such difference may be traced down to the difference in chemical properties between Sn⁴⁺ and the other two ions of the same group. It is noted that the VRBE for the VBM from the hybrid DFT calculations is α dependent, and the obtained values here lie beneath those of the empirical model [11], while the values from PBE calculation are above those of the empirical model. If the VRBE of the VBM from the PBE calculation was employed, the $\epsilon(+2/+1)$ of CaSnO₃:Bi³⁺ would be slightly higher than those in the two other hosts, as plotted in Fig. S9 in the SM [29]. This indicates that the hole traps of Bi³⁺ $6s$ character in the three hosts might actually align with each other even better than those reported in Fig. 4.

In Ref. [11], Awater and Dorenbos concluded that the VRBE of Bi³⁺ $6s$ is strongly connected to the nephelauxetic effect, which is closely related to the coordination numbers and the average bond length of the polyhedron in CaMO₃:Bi³⁺ and becomes stronger with decrease in coordination number and shrinkage of the bond length [47]. This is partially confirmed by our calculation: compared to CaZrO₃, the slight decrease of the average bond length lifts the VRBE of the Bi-activated hole trap in CaTiO₃ by 0.13 eV. However, the VRBE of Bi³⁺ $6s$ orbital in CaSnO₃ is the lowest among the three hosts, although its bond length is larger than that in CaTiO₃. This indicates that M^{4+} ion has some impacts on the nephelauxetic effect.

D. Luminescence mechanism of the three materials

Experimentally measured photoluminescent spectra for the three phosphors show quite different features. Based on our results on the charge transition levels, we attribute them to Bi³⁺-related transitions. The CaTiO₃:Bi³⁺ and CaSnO₃:Bi³⁺ exhibit much broader emission bands than CaZrO₃:Bi³⁺. The full width at half maximum (FWHM) is 0.57 eV [18], 0.59 eV [19], and 0.31 eV [20] for $M = \text{Ti, Sn, and Zr}$, respectively. Meanwhile, at a low temperature, a weak band near 360 nm (3.44 eV) shows up in the emission spectrum of CaSnO₃:Bi³⁺. The measured excitation spectrum of CaTiO₃:Bi³⁺ [18] is characterized by a structured broad band dominated in the range of 250–400 nm, which is featured by a peak at 320 nm, a shoulder around 375 nm, and a short-wavelength cutoff around 250 nm. For CaSnO₃:Bi³⁺, there are mainly two ex-

TABLE III. Calculated and measured excitation and emission energies of MMCT, A band, and CT in CaMO₃ perovskites ($M = \text{Zr, Sn, Ti}$) in units of eV. Data in parentheses are calculated emissions that are not observable in experiment.

		MMCT		A band		CT	
		Ex	Em	Ex	Em	Ex	Em
CaTiO ₃	calc.	3.05	2.22	3.69 ^a		4.72 ^a	
	expt.	3.31	2.23	3.88	$\sim 2.80^b$	4.56	
CaSnO ₃	calc.	3.78	2.86	3.99 ^a	3.47 ^a	6.08 ^a	(4.05)
	expt.	~ 4.03	2.74	4.03	3.44		
CaZrO ₃	calc.	5.19	(4.18)	4.10	3.15	5.50	(3.59)
	expt.	5.23		3.92	3.18	5.70	

^aTransition energies approximated by using energies of unoccupied GKS orbitals.

^bThe emission band measured under 3.75-eV excitation given in the Supporting Information of Ref. [12].

citation bands peaking at 308 and 260 nm [20,21], with some less-resolved features between the two broad excitation bands [12]. The CaZrO₃:Bi³⁺ compound exhibits a more structured excitation spectrum, including one narrow band peaking at 304 nm [21] (FWHM of ~ 0.48 eV) and a broad band dominated in the range from 5.0 to 5.8 eV [12].

Based on the optimized equilibrium structures for both ground and various Bi³⁺-related excited states for all three hosts, we obtain the excitation and emission energies for various transitions, as listed in Table III. In order to show the dynamical processes, a schematic configurational coordinate diagram is constructed based on these data (Fig. 5). In CaTiO₃:Bi³⁺, the calculated energy of the MMCT excitation is 3.05 eV, which matches the unidentified 375-nm shoulder in the excitation spectrum (Ref. [18]). The calculated energies of A band and CT excitations are 3.69 and 4.72 eV, respectively, and they match the peak of 320 nm (3.88 eV) and ~ 272 nm (4.56 eV) in the measured excitation spectrum (Ref. [18]), respectively. The band gap of CaSnO₃ is 1.36 eV larger than that of CaTiO₃, and it results in the upward shift of the CBM towards the ${}^3P_{0,1}$ as shown in Fig. 5(b). The calculation for CaSnO₃:Bi³⁺ given in Table III shows that the MMCT and A band excitations are centered at 3.78 and 3.99 eV. The calculated excitation energy difference between the MMCT and the A band is only 0.22 eV and the absorption of MMCT is expected to be blurred by the strong parity-allowed ${}^1S_0 \rightarrow {}^3P_1$ excitation. This corresponds to the excitation band observed around 4.03 eV in Ref. [19]. The calculated CT excitation band is at 6.08 eV, much higher than the edge of band-to-band absorption, and presumably is blurred by interband absorption. The band gap of CaZrO₃ is even larger (5.94 eV), and the MMCT excitation energy is calculated to be 1.09 eV higher than the A band transition. In above calculations of the three materials, the predicted MMCT excitation energies are systematically lower by about 0.2 eV than the measured MMCT bands. We note that the calculated values are only the low bound of the vertical ionization of an electron from Bi³⁺ to CB, which is expected to be lower than the peak energy of MMCT bands. Significantly, the variation of the

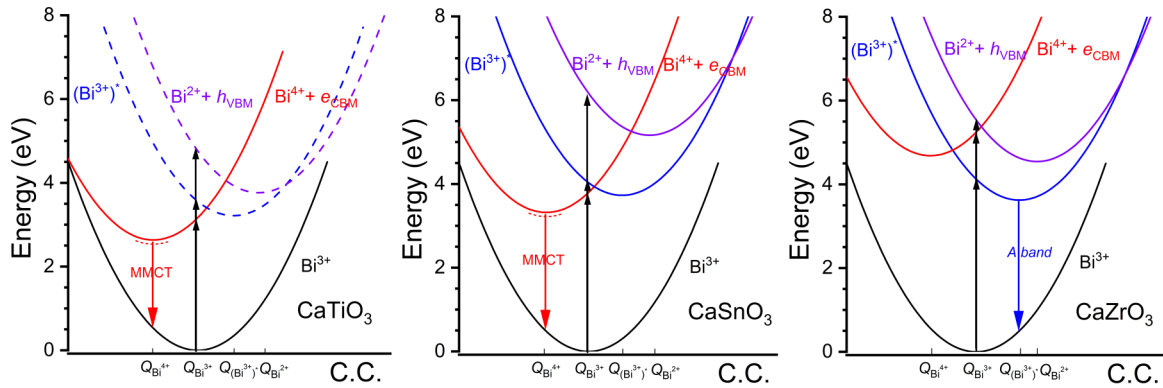


FIG. 5. Configurational coordinate diagrams of the defects' potential surfaces as a function of the generalized configuration coordinate for CaMO_3 perovskites ($M = \text{Zr}, \text{Sn}, \text{Ti}$). Notes: (1) Bi^{3+} and $(\text{Bi}^{3+})^*$ denote the ground and ${}^3P_{0,1}$ excited states of Bi^{3+} in the host, respectively. (2) $\text{Bi}^{4+} + e_{\text{CBM}}$ simulates Bi^{4+} with an electron at CBM, representing the lowest MMCT excited state. (3) $\text{Bi}^{2+} + h_{\text{VBM}}$ simulates Bi^{2+} with a loose hole at VBM, representing the lowest CT excited state. (4) Energy surfaces for $(\text{Bi}^{3+})^*$ and $\text{Bi}^{2+} + h_{\text{VBM}}$ in CaTiO_3 are estimated by referring to CaZrO_3 for energy relaxation and are drawn in dashed lines for reference only.

relative positions of the MMCT and the A band excitation with the band gap in $\text{CaMO}_3 : \text{Bi}^{3+}$ shows great consistency with the three situations of the CBM and ${}^3P_{0,1}$ energy level patterns introduced in Ref. [14].

The MMCT excitations of $\text{CaMO}_3 : \text{Bi}^{3+}$ were evaluated previously with the semiempirical method in Ref. [12]. It considered the electronegativity of different M^{4+} and the shortest distance between the M^{4+} site and the Ca^{2+} site (d_{corr}) that includes the ionic radius differences due to replacing Ca^{2+} by Bi^{3+} . The effect of the charge difference between Bi^{3+} and Ca^{2+} is neglected in the distance correction. In our calculation, the bond lengths turned out to be hardly changed by Bi^{3+} substitution. Meanwhile, the d_{corr} is expected to have little influence on the MMCT excitation energies, because even the d_{corr} in CaSnO_3 , which is predicted to be the largest among the three, is merely 2.1% ($\sim 0.05 \text{ \AA}$) larger than in CaTiO_3 , the smallest among the three. Thus, the MMCT excitation results from this empirical method are mostly differentiated by the electronegativity of different M^{4+} . The result is very close to the measurement in $\text{CaSnO}_3 : \text{Bi}^{3+}$ but is overestimated by 0.46 eV in $\text{CaTiO}_3 : \text{Bi}^{3+}$ and significantly underestimated by 1.31 eV in $\text{CaZrO}_3 : \text{Bi}^{3+}$. The A band excitation has also been evaluated empirically based on the environmental factor involving the chemical bonds between the central ion and the nearest anions. Since those parameters are similar in the three CaMO_3 hosts, the predicted excitation energies are quite similar in the three materials, remarkably different from the measurements and our first-principles calculations.

With the calculated equilibrium structures for various excited states, we obtained the emission energies for possible transitions and their Stokes shifts. The Bi^{3+} 6s orbitals are all above the VBM in three CaMO_3 , thus the CT emissions are expected to be higher in energy than ${}^3P_{0,1}$ and not observable. Only in CaZrO_3 the Bi^{3+} 6p orbital is lower than the CBM, and the emission cannot be dominated by the ${}^3P_{0,1}$ emission in the other two materials. The calculated MMCT emissions in $\text{CaTiO}_3 : \text{Bi}^{3+}$ and $\text{CaSnO}_3 : \text{Bi}^{3+}$ are 2.22 and 2.86 eV, respectively. These values are consistent with the peaks 2.23 and 2.73 eV from the measured broad emis-

sion band listed in Table III. Furthermore, in $\text{CaSnO}_3 : \text{Bi}^{3+}$, there is an extra weak low-temperature emission band at 3.44 eV, which is attributed to the A band emission calculated at 3.47 eV. This indicates that the metastable ${}^3P_{0,1}$ excited state above the MMCT state becomes emissive at low temperature, and the large coordination difference between those two excited states hindered the prompt relaxation from ${}^3P_{0,1}$ to the MMCT state. In both CaTiO_3 and CaSnO_3 , the A band and MMCT excitations overlap and the origin of the Bi^{3+} emitting could be ambiguous, since the $(\text{Bi}^{3+})^*$ excited state could transfer to $\text{Bi}^{4+} + e_{\text{CBM}}$ or vice versa depending on their relative position. The actual emissive level is the lower one of the two excited levels after structure relaxation, which is resolved to be MMCT here by the first-principles calculations. In addition, our calculation reveals that the CT excited states tend to relax to the $(\text{Bi}^{3+})^*$ excited state beneath it. As for $\text{CaZrO}_3 : \text{Bi}^{3+}$, the ${}^3P_{0,1}$ and CT states are all located in the band gap, and the emission is dominated by the lowest excited state. The calculated A band excitation and emission energies are 4.10 and 3.15 eV, respectively, which are consistent with the measured spectra. In comparison, the A band excitation energy, obtained approximately from the GKS eigenvalues at 3.84 eV in the hybrid DFT + SOC calculation of $\text{CaZrO}_3 : \text{Bi}^{4+}$, is slightly underestimated compared to the one from total energy difference (4.10 eV). The calculated MMCT and CT excitation in $\text{CaZrO}_3 : \text{Bi}^{3+}$ agree quite well with the two peaks 5.23 and 5.70 eV resolved from a super-broad excitation band ranging from 5 to 6 eV in Ref. [12]. However, those two excited states are not metastable and their excitations will rapidly relax to the ${}^3P_{0,1}$ excited state to emit [Fig. 5(c)].

To sum up, M^{4+} ions have a strong effect on the relative position of the excited states, the excitation and emission spectra, and luminescent dynamical processes of $\text{CaMO}_3 : \text{Bi}^{3+}$. The band gap of CaZrO_3 is large enough to contain the ${}^3P_{0,1}$ excited state, which dominates both the absorption and emission, while the smaller band gaps in CaSnO_3 and CaTiO_3 make the ${}^3P_{0,1}$ and CT excited states not stable, resulting in the emission from MMCT excited states.

E. Further discussions on Bi^{3+} in other hosts with similar environment

We have also performed the calculation for $\text{CaHfO}_3:\text{Bi}^{3+}$. The lowest excited state is predicted to be ${}^3P_{0,1}$, and the excitation and emission energies are 3.94 and 2.86 eV, respectively. This agrees with the assignment and peak energies [48]. Based on our first-principles studies for $\text{CaMO}_3:\text{Bi}^{3+}$, the luminescent mechanisms of $\text{SrMO}_3:\text{Bi}^{3+}$ ($M = \text{Sn, Zr}$) can be readily inferred without resorting to sophisticated calculations as follows. Similar to $\text{CaSnO}_3:\text{Bi}^{3+}$, the emission of $\text{SrSnO}_3:\text{Bi}^{3+}$ is dominated by a broad band with a large Stokes shift, which can be assigned as the MMCT emission, and a narrow emission due to ${}^3P_{0,1}$ emission was observed at low temperature [49]. The same phenomenon is expected in $\text{SrTiO}_3:\text{Bi}^{3+}$, but no experimental results are available for comparison. Regarding $\text{SrZrO}_3:\text{Bi}^{3+}$, the lowest excited state is expected to be ${}^3P_{0,1}$, giving a narrow emission band [49]. Since the ion radius of Sr^{2+} is larger than that of Ca^{2+} , a larger structure relaxation of the Bi^{3+} dopant is expected, which explains the slightly larger broadening of the emission and larger Stokes shift.

IV. CONCLUSION

In this work, hybrid DFT calculations have been performed to study the luminescence mechanisms of the Bi^{3+} doped CaMO_3 perovskites ($M = \text{Zr, Sn, Ti}$). The geometric structures for both the ground states and excited states were obtained with proper treatments of the electron configuration of Bi^{3+} ions. Based on these geometric structures, a clear diagram of all the levels involved in the photoluminescent processes has been obtained. The calculated results show that the luminescence is due to A band transition in $\text{CaZrO}_3:\text{Bi}^{3+}$ but MMCT transition in $\text{CaSnO}_3:\text{Bi}^{3+}$ and $\text{CaTiO}_3:\text{Bi}^{3+}$, with calculated emission energies and Stokes shifts matching

experimental measurements very well. The main features in the excitation spectra have all been reliably assigned to A band, MMCT, and CT transitions by matching calculated to measured peak energies for Bi^{3+} in all three hosts. The A band excitation is always dominant at similar energies in the three $\text{CaMO}_3:\text{Bi}^{3+}$, while the MMCT excitations vary with the upshift of the CBM along $M = \text{Ti, Sn, to Zr}$. As for the CT excitation, the $6p$ level of Bi^{2+} is located in the band gap only for CaZrO_3 , but is scattered high up in CBs in CaSnO_3 and CaTiO_3 . Our calculations on the trap depths predict that Bi^{3+} can work as both hole and electron traps in CaZrO_3 , but only hole traps in the CaTiO_3 and CaSnO_3 . Interestingly, different from the usual expectation that all the Bi-O bond lengths vary almost simultaneously when Bi^{3+} is excited to $\text{Bi}^{4+} + e_{\text{CB}}$, $\text{Bi}^{2+} + h_{\text{VB}}$ or $(\text{Bi}^{3+})^*$, some bond lengths vary dramatically while others are barely changed. Our study has clearly demonstrated the potential of the proposed calculation scheme in predicting and analyzing the properties of Bi^{3+} activated luminescent materials, which will benefit the design and optimization of new phosphors.

ACKNOWLEDGMENTS

The numerical calculations in this paper were partially performed on the supercomputing system in the Supercomputing Center of University of Science and Technology of China. This work was financially supported by the National Key Research and Development Program of China (Grants No. 2018YFA0306600 and No. 2016YFB0701001), the National Natural Science Foundation of China (Grants No. 61635012 and No. 11974338), and University Science Research Project of Anhui Province (Grant No. KJ2017A791). Y.-Y.Y. also gratefully acknowledges financial support from the Committee on Research and Development and Dean's Research Grants of the Faculty of Liberal Arts and Social Sciences of the Education University of Hong Kong.

-
- [1] H. Shao, X. Bai, H. N. Cui, G. C. Pan, P. T. Jing, S. N. Qu, J. Y. Zhu, Y. Zhai, B. Dong, and H. W. Song, *Nanoscale* **10**, 1023 (2018).
- [2] X. Y. Huang, L. Xiong, L. Yu, X. H. Gao, and X. Q. Qiu, *Inorg. Chem.* **59**, 7752 (2020).
- [3] M. Amiri, N. P. Martin, O. Sadeghi, and M. Nyman, *Inorg. Chem.* **59**, 3471 (2020).
- [4] W. C. Wang, B. Zhou, S. H. Xu, Z. M. Yang, and Q. Y. Zhang, *Prog. Mater. Sci.* **101**, 90 (2019).
- [5] Z. L. Li, Y. Hu, K. A. Howard, T. T. Jiang, X. L. Fan, Z. H. Miao, Y. Sun, F. Besenbacher, and M. Yu, *Acs Nano* **10**, 984 (2016).
- [6] D. J. Liu, X. H. Yun, P. P. Dang, H. Z. Lian, M. M. Shang, G. G. Li, and J. Lin, *Chem. Mater.* **32**, 3065 (2020).
- [7] H. C. Swart and R. E. Kroon, *Opt. Mater.: X* **2**, 100025 (2019).
- [8] P. Dang, D. Liu, G. Li, A. A. Al Kheraif, and J. Lin, *Adv. Opt. Mater.* **8**, 1901993 (2020).
- [9] A. Krasnikov, E. Mihokova, M. Nikl, S. Zazubovich, and Y. Zhdachevskyy, *Crystals* **10**, 208 (2020).
- [10] W. V. Houston, *Phys. Rev.* **33**, 297 (1929).
- [11] R. H. P. Awater and P. Dorenbos, *J. Lumin.* **184**, 221 (2017).
- [12] M. Back, J. Ueda, J. Xu, K. Asami, L. Amidani, E. Trave, and S. Tanabe, *J. Phys. Chem. C* **123**, 14677 (2019).
- [13] P. Boutinaud, *Inorg. Chem.* **52**, 6028 (2013).
- [14] M. Amer and P. Boutinaud, *Phys. Chem. Chem. Phys.* **19**, 2591 (2017).
- [15] P. Boutinaud, *J. Lumin.* **223**, 117219 (2020).
- [16] F. Kang, H. Zhang, L. Wondraczek, X. Yang, Y. Zhang, D. Y. Lei, and M. Peng, *Chem. Mater.* **28**, 2692 (2016).
- [17] M. Colmont, P. Boutinaud, C. Latouche, F. Massuyeau, M. Huve, A. Zadoya, and S. Jobic, *Inorg. Chem.* **59**, 3215 (2020).
- [18] R. P. Cao, T. Fu, H. D. Xu, W. J. Luo, D. D. Peng, Z. Q. Chen, and J. W. Fu, *J. Alloys Compd.* **674**, 51 (2016).
- [19] R. P. Cao, J. L. Zhang, W. D. Wang, Q. L. Hu, W. S. Li, W. Ruan, and H. Ao, *Luminescence* **32**, 908 (2017).
- [20] A. M. Srivastava, *Opt. Mater.* **58**, 89 (2016).
- [21] P. Stoch, J. Szczerba, J. Lis, D. Madej, and Z. Pedzich, *J. Eur. Ceram. Soc.* **32**, 665 (2012).
- [22] M.-H. Du, *ECS J. Solid State Sci. Technol.* **5**, R3007 (2016).

- [23] Y. C. Jia, S. Ponce, A. Miglio, M. Mikami, and X. Gonze, *Adv. Opt. Mater.* **5**, 1600997 (2017).
- [24] L. X. Ning, X. X. Huang, Y. C. Huang, and P. A. Tanner, *J. Mater. Chem. C* **6**, 6637 (2018).
- [25] J. J. Cai, W. G. Jing, J. Cheng, Y. F. Zhang, Y. H. Chen, M. Yin, Y.-Y. Yeung, and C.-K. Duan, *Phys. Rev. B* **99**, 125107 (2019).
- [26] G. Kresse and J. Furthmüller, *Phys. Rev. B* **54**, 11169 (1996).
- [27] G. Kresse and D. Joubert, *Phys. Rev. B* **59**, 1758 (1999).
- [28] P. E. Blochl, *Phys. Rev. B* **50**, 17953 (1994).
- [29] See Supplemental Material at <http://link.aps.org/supplemental/10.1103/PhysRevB.103.075109> for the details of the discussions of the influence of the single Γ point, charge corrections and site occupations of Bi³⁺ ions, some extra data on the properties of the excited states, transition energies based on GKS eigenvalues, and vacuum referenced binding energies of the defects, which includes Refs. [30–36].
- [30] G. Makov and M. C. Payne, *Phys. Rev. B* **51**, 4014 (1995).
- [31] S. Lany and A. Zunger, *Phys. Rev. B* **78**, 235104 (2008).
- [32] C. Freysoldt, J. Neugebauer, and C. G. Van de Walle, *Phys. Rev. Lett.* **102**, 016402 (2009).
- [33] T. R. Durrant, S. T. Murphy, M. B. Watkins, and A. L. Shluger, *J. Chem. Phys.* **149**, 024103 (2018).
- [34] E. Cockayne and B. P. Burton, *Phys. Rev. B* **62**, 3735 (2000).
- [35] W. W. Coffeen, *J. Am. Ceram. Soc.* **36**, 207 (1953).
- [36] C. Xing, J. Wang, J. Li, and F. Shi, *J. Adv. Dielectrics* **8**, 1850029 (2018).
- [37] W. Setyawan and S. Curtarolo, *Compos. Mater. Sci.* **49**, 299 (2010).
- [38] D. Koller, F. Tran, and P. Blaha, *Phys. Rev. B* **85**, 155109 (2012).
- [39] P. Blaha, K. Schwarz, F. Tran, R. Laskowski, G. K. H. Madsen, and L. D. Marks, *J. Chem. Phys.* **152**, 074101 (2020).
- [40] J. P. Perdew, M. Ernzerhof, and K. Burke, *J. Chem. Phys.* **105**, 9982 (1996).
- [41] M. A. L. Marques, J. Vidal, M. J. T. Oliveira, L. Reining, and S. Botti, *Phys. Rev. B* **83**, 035119 (2011).
- [42] M. Gerosa, C. E. Bottani, L. Caramella, G. Onida, C. Di Valentin, and G. Pacchioni, *Phys. Rev. B* **91**, 155201 (2015).
- [43] P. Deak, Q. Duy Ho, F. Seemann, B. Aradi, M. Lorke, and T. Frauenheim, *Phys. Rev. B* **95**, 075208 (2017).
- [44] D. Hobbs, G. Kresse, and J. Hafner, *Phys. Rev. B* **62**, 11556 (2000).
- [45] C. Freysoldt, B. Grabowski, T. Hickel, J. Neugebauer, G. Kresse, A. Janotti, and C. G. Van de Walle, *Rev. Mod. Phys.* **86**, 253 (2014).
- [46] G. Miceli, W. Chen, I. Reshetnyak, and A. Pasquarello, *Phys. Rev. B* **97**, 121112(R) (2018).
- [47] X. Li, P. L. Li, Z. J. Wang, S. M. Liu, Q. Bao, X. Y. Meng, K. L. Qiu, Y. B. Li, Z. Q. Li, and Z. P. Yang, *Chem. Mater.* **29**, 8792 (2017).
- [48] A. A. Setlur and A. M. Srivastava, *Opt. Mater.* **29**, 410 (2006).
- [49] A. M. Srivastava, *Opt. Mater.* **72**, 313 (2017).
- [50] I. Levin, T. G. Amos, S. M. Bell, L. Farber, T. A. Vanderah, R. S. Roth, and B. H. Toby, *J. Solid State Chem.* **175**, 170 (2003).